IEEE Transactions on Nuclear Science, Vol. NS-30, No. 4, August 1983

PULSED AIR-CORE DEFLECTOR-MAGNET DESIGN PARAMETERS*

Andrew J. Jason, Richard K. Cooper, Aaron D. Liebman, Barbara Blind, and Alfred R. Koelle, AT-3, MS H808
Los Alamos National Laboratory, Los Alamos, NM 87545

Summary

The response of air-core magnets to pulsed excitation is dependent on the pulse frequency spectrum because of fields produced by induced currents in the magnet structure. We discuss this phenomenon quantitatively in terms of magnet performance optimization.

Introduction

The Los Alamos Proton Storage Ring (PSR) uses pulsed inflector magnets to distort the stored-beam orbit during accumulation to minimize interaction with an injection stripping foil and to manipulate beam phase-space distributions. For the high-intensity pulsed PSR beam, it was considered desirable to avoid using ferrite magnets in the ring to preclude reactive effects. An alternative, air-core magnets, provides lower inductances than ferrite-loaded structures but requires higher drive currents and has a more complex response to the drive frequency spectrum. Application of inflector magnets to the PSR and possible driver-circuitry design has been discussed.[1] Here we relate study results of a particular magnet form suitable for pulsed operation with several kiloamperes drive current and response times of several microseconds.

Magnet Description

The magnet type we discuss is shown in Fig. 1, where the relevant dimensions are defined. The magnet consists of one rectangularly formed turn with apertures in the ends for beam passage. The longitudinal electrodes have a radius on their inner surface for control of field homogeneity and the assembly is contained in a cylindrical vacuum chamber with radius R and thickness t. Although other configurations may be advantageous, the assembly shown in Fig. 1 features low inductance, ease of construction, and is capable of high duty factors. A prototype has been constructed with dimensions as given in Fig. 1. The copper sections were pinned together and heliarc brazed. The parallel-strip structure of the magnet leads is continued with the vacuum feedthrough and strip-line conductors for current transmission from the driver. The magnet's low-frequency inductance is ~0.3 μH and the dc resistance is 40 μΩ.

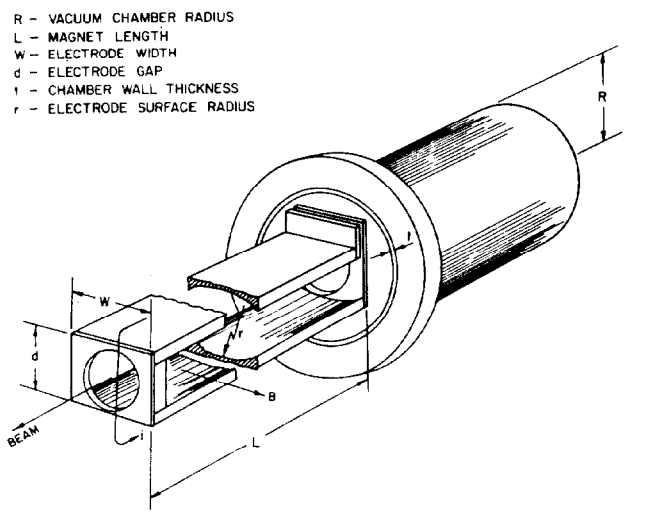

Fig. 1. Type of single-turn magnet considered here. A prototype magnet was built with R = 7.2 cm, L = 48 cm, d = 7.6 cm, w = 10.5 cm and t = 0.2 cm. The measurements quoted in the text refer to this magnet. The chamber is stainless steel and the electrodes are copper, 1 cm thick at the edges.

Magnet Pulsed Behavior

The frequency dependence of the field's real and imaginary parts for a unit drive current specifies the magnet frequency spectrum. We determine the spectrum by a theoretical model, and then are able to calculate the field produced for a specified current waveform. The results show a frequency-dependent response.

Solution of the Diffusion Equation

We consider the simplified two-dimensional model of the magnet shown in Fig. 2. Two very thin electrodes with symmetry about the x- and y-axes have equal and opposite currents flowing perpendicular to the figure and produce a field along the y-axis. Two infinite parallel conducting sheets of thickness t and conductivity σ are located at y = ±h.

Neglecting displacement currents, the diffusion equation for a given frequency ω is

$$\frac{\partial^2 A_z}{\partial x^2} + \frac{\partial^2 A_z}{\partial y^2} - i\mu_o \sigma \omega A_z = 0 \quad , \tag{1}$$

where A_z is the vector potential. The solution for the vector potential expanded in terms of the appropriate eigenfunctions with the conducting sheets at y = ±h removed is

$$A_z = \int_0^\infty dk\, a(k)\, e^{-ky} \sin kx \quad , \tag{2}$$

for y > 0. A symmetric expression applies for y < 0. We assume that a(k) is determined by solution of Eq. (1) or from boundary conditions at the electrodes; several such configurations are analytically soluble.

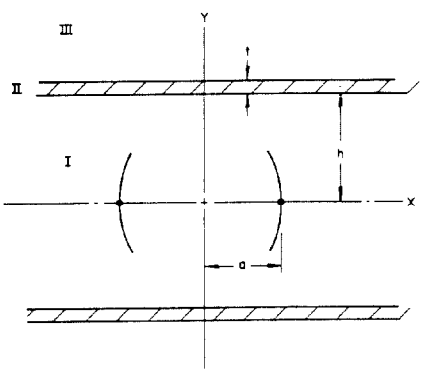

Fig. 2. Simplified magnet model for magnet-frequency spectra analysis.

*Work supported by the US Department of Energy.

0018-9499/83/0800-2938$01.00©1983 IEEE

We next decompose the vector potential for the full problem into two terms: the potential of the electrodes alone and the change in potential caused by the currents induced in the sheets. Call this latter term A_z^i. The induced field is expanded in the form

$$A_z^i = \int_0^\infty dk\, A(k,y) \sin kx \quad . \tag{3}$$

Substitution in Eq. (1) gives

$$\frac{\partial^2 A(k,y)}{\partial y^2} - \beta^2 A(k,y) = - i\mu_0\sigma\omega e^{-ky}\, a(k) \quad , \tag{4}$$

where $\beta^2 = k^2 - i\mu_0\sigma\omega$. The solutions of Eq. (4) are, for the respective regions I, II, and III (Fig. 2),

$$A^I(k,y) = b(k) \cosh ky \quad ,$$

$$A^{II}(k,y) = \alpha_1(k)e^{-\beta y} + \alpha_2(k)e^{\beta y} + e^{-ky}\, a(k) \quad , \tag{5}$$

and

$$A^{III}(k,y) = c(k)e^{-ky} \quad .$$

Equating solutions and derivatives at the sheet boundaries ($y = h$ and $y = h + t$), we obtain four equations in the four coefficients of relations in Eq. (5). Solving for b(k) we find

$$b(k) = a(k)e^{-kh}\, \frac{\cosh ky}{\cosh kh}\, \frac{1 - \gamma}{1 + \gamma \tanh kh} \quad , \tag{6}$$

where $\gamma = (1 + k/\beta \tanh \beta t)/(1 + \beta/k \tanh \beta t)$.

For numerical results, we consider the electrodes in Fig. 2 to be shrunk to points at $x = \pm a$, $y = 0$. For unit drive current, this gives

$$a(k) = \frac{\mu_0}{\pi k} \sin ka \quad . \tag{7}$$

Substituting Eqs. (6) and (7) into Eq. (3), we find a complex expression for the induced field as a function of frequency, conductivity, magnet dimensions, and coordinates. Evaluation shows weak dependence of the frequency spectrum form on electrode shape.

Magnet Frequency Spectrum

Considerations of the preceding section give the form of the field produced by the induced wall currents. Magnitudes will depend strongly on geometry but we find that form does not. To predict the response of a given magnet to a current drive as a function of frequency, we first calculate the fields at low and high frequency using the magnet code POISSON and then normalize to the calculated spectrum.

Results of this procedure for the prototype magnet (assuming the wall conductivity is that of stainless steel) are shown in Fig. 3. The experimental points were obtained with a small coil centered in the magnet and monitored by a lock-in amplifier. Measurements also were taken using a large coil, which integrated over the entire magnet length, with similar results. A small frequency effect (~6%) is seen for the bare magnet, that is, the assembly in Fig. 1 with the vacuum chamber removed. Full scale in the figure corresponds to a field of 63 G/kA.

The decrease in field with frequency for the bare magnet is caused by the redistribution of currents in the magnet electrodes, that is, an increase in current density toward the edges and inner surfaces. This effect is not predicted by our calculations because a definite current distribution is assumed. Addition of the vacuum chamber increases the frequency dependence; the magnet field is opposed by the wall currents it induces. The high frequency attentuation increases with vacuum-chamber proximity and wall thickness. The region in which the spectrum changes sharply, moves toward lower frequencies with increasing conductivity; the inflection point in the real part of the plot occurs at the frequency for which the skin depth is approximately half the wall thickness.

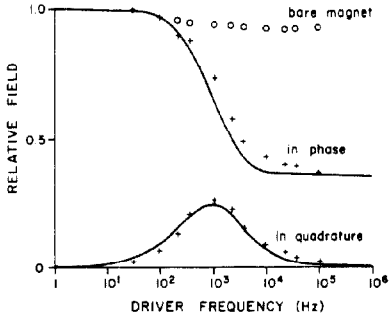

Fig. 3. In-phase and quadrature parts of the relative field (in the magnet center) as a function of frequency. Solid lines are calculated values whereas the crosses are pickup-coil results for the magnet described in Fig. 1. The points labeled "bare magnet" are for the same magnet but removed from its vacuum chamber.

Pulse Distortion

Given the frequency spectrum, it is straightforward to predict the field produced by a given drive pulse; the input current is Fourier analyzed and folded into the spectrum. In Fig. 4 we show results of such a calculation for a magnet with the prototype dimensions and driven by a pulse whose rise is a pure exponential and whose fall is a linear combination of exponentials. The waveform is severely distorted from the shown linear response. Magnet response is such that the field amplitude is attenuated and the pulse tail is extended. The remedy for such distortion is to decrease wall thickness and to increase chamber radius; the high frequency attenuation then decreases asymptotically to the bare magnet case. For a vacuum chamber with diameter 2.5 times w (the magnet width),

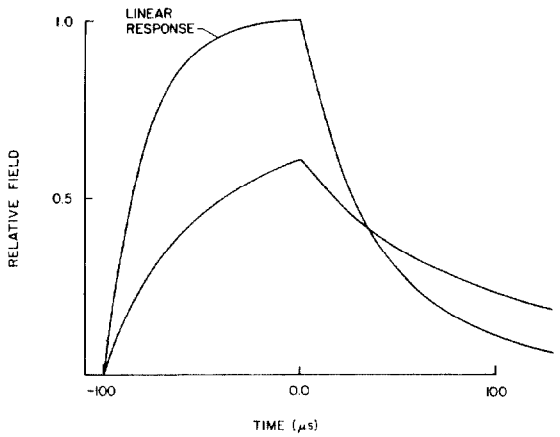

Fig. 4. Relative fields versus time for an input-current waveform proportional to the upper curve that shows the linear response. The lower curve shows the response of the prototype magnet.

the pulse amplitude distortion is <12%. Of course if time scales are decreased, the distortion will be correspondingly greater. Additionally, distortion will occur if conducting or ferromagnetic surfaces are placed near the magnet.

Magnet Electrical Parameters

Figure 5 shows a terminal equivalent circuit for the magnet, which is merely the schematic equivalent for a transformer with primary inductance L_1 and resistance R_1 (representing the bare magnet) and secondary with corresponding parameters L_2 and R_2 (representing the inductance and effective resistance of the chamber walls). Coupling between the circuits is described by the mutual inductance, M. The impedance of this circuit is

$$Z = R_1 + \frac{R_2 M^2\omega^2}{R_2^2 + \omega^2 L_2^2} + j\omega\left(L_1 - \frac{L_2 M^2\omega^2}{R_2^2 + \omega^2 L_2^2}\right) \quad ; \qquad (8)$$

the fit to the parameters in Eq. (8) was obtained from asymptotic measurements and the frequency spectrum. For the prototype magnet, R_2 = 1400 μΩ, L_2 = 0.33 μH, and M = 0.21 μH (increasing the chamber radius to 13 cm reduces M to 0.04 μH). This result is shown in Fig. 5, where adjustment has been made for variation of conductor resistance with frequency.

Field Homogeneity

A plot of data from measurements taken with a small coil that was moved along the magnet axis is shown in Fig. 6. The effective length of the magnet (based on the central field) is ∿6% less than the physical length. The field cuts off sharply at the ends and has an (expected) bump at the ends that increases with frequency.

Figure 7 shows POISSON calculations for the ratio of the sextupole field at the electrode radius to the dipole field, using the prototype geometry. The sextupole is defined here as positive when its field adds to the dipole field along an axis perpendicular to the electrodes. For very large electrode radius, r, the prototype magnet sextupole is ∿15%. These

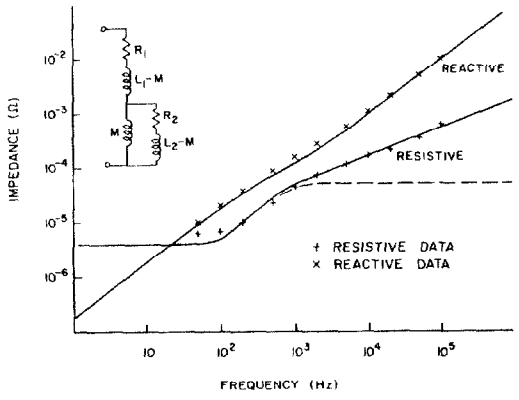

Fig. 5. Magnet equivalent circuit and plot of impedances as a function of frequency. The solid line is a semiempirical fit to the circuit whereas the points are measurements. The dashed line is the impedance obtained directly from Eq. (8); the solid line has been analytically corrected for conductor skin effect.

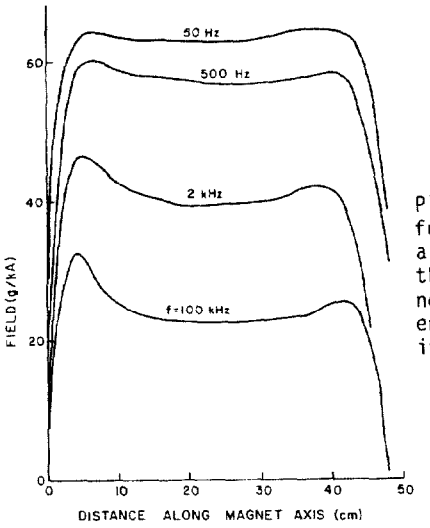

Fig. 6. Plot of field as a function of distance along the axis for the prototype magnet. The lead-in end is to the left in the figure.

values do not include the end sextupole, which is negative. However, measurements with a Morgan coil,[2] which integrated over the entire magnet length, qualitatively confirm the sextupole behavior and magnitude implied by the plot in Fig. 7 except for an anomalous increase at high frequencies. Close cancellation of the net sextupole is difficult, but may be approached by shaping the electrodes for a larger dc current density at the electrode edges. This will bring the dc and intermediate frequency sextupoles closer in value. The value and sign then can be adjusted to cancel the end sextupole by further shaping. Higher order harmonics may need adjustment for certain applications. The high-frequency inhomogeneity is a wall effect and can be minimized with a large chamber radius.

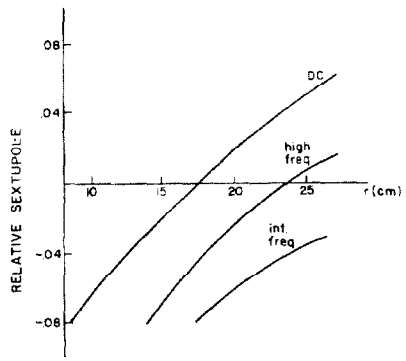

Fig. 7. Relative sextupole as a function of electrode radius, r, from POISSON calculations. In the intermediate frequency case, we set the electrode vector potential constant. Additionally, for the high-frequency result, the field does not penetrate the walls.

References

1. A. Jason, E. Higgins, and A. Koelle, "The Los Alamos Proton Storage Ring Injection Deflector System," Los Alamos National Laboratory document LAUR-83-719 (1983).

2. G. Morgan, "Stationary Coil for Measuring the Harmonics in Pulsed Transport Magnets," Proc. 4th Int. Conf. on Magnet Tech., Brookhaven National Laboratory, Upton, New York, September 19, 1972, Brookhaven National Laboratory report CONF-720908, p. 787 (1972).